MIT Open Access Articles

THE INTRINSIC SHAPE OF SAGITTARIUS A* AT 3.5 mm WAVELENGTH

THE INTRINSIC SHAPE OF SAGITTARIUS A* AT 3.5 mm WAVELENGTH

Gisela N. Ortiz-León[1], Michael D. Johnson[2], Sheperd S. Doeleman[2,3], Lindy Blackburn[2], Vincent L. Fish[3], Laurent Loinard[1,4], Mark J. Reid[2], Edgar Castillo[5,9], Andrew A. Chael[2], Antonio Hernández-Gómez[1], David H. Hughes[5], Jonathan León-Tavares[5,6], Ru-Sen Lu[4], Alfredo Montaña[5,9], Gopal Narayanan[7], Katherine Rosenfeld[2], David Sánchez[5], F. Peter Schloerb[7], Zhi-qiang Shen[8], Hotaka Shiokawa[2], Jason SooHoo[3], and Laura Vertatschitsch[2]

[1] Instituto de Radioastronomía y Astrofísica, Universidad Nacional Autónoma de México, Morelia 58089, México; g.ortiz@crya.unam.mx
[2] Harvard-Smithsonian Center for Astrophysics, 60 Garden Street, Cambridge, MA 02138, USA
[3] Massachusetts Institute of Technology, Haystack Observatory, Route 40, Westford, MA 01886, USA
[4] Max Planck Institut für Radioastronomie, Auf dem Hügel 69, D-53121 Bonn, Germany
[5] Instituto Nacional de Astrofísica Óptica y Electrónica, Apartado Postal 51 y 216, 72000 Puebla, México
[6] Sterrenkundig Observatorium, Universiteit Gent, Krijgslaan 281-S9, B-9000 Gent, Belgium
[7] Department of Astronomy, University of Massachusetts, Amherst, MA 01002, USA
[8] Shanghai Astronomical Observatory, 80 Nandan Road, Shanghai 200030, China
Received 2016 January 25; accepted 2016 March 14; published 2016 June 8

ABSTRACT

The radio emission from Sgr A* is thought to be powered by accretion onto a supermassive black hole of $\sim 4 \times 10^6 \, M_\odot$ at the Galactic Center. At millimeter wavelengths, Very Long Baseline Interferometry (VLBI) observations can directly resolve the bright innermost accretion region of Sgr A*. Motivated by the addition of many sensitive long baselines in the north–south direction, we developed a full VLBI capability at the Large Millimeter Telescope Alfonso Serrano (LMT). We successfully detected Sgr A* at 3.5 mm with an array consisting of six Very Long Baseline Array telescopes and the LMT. We model the source as an elliptical Gaussian brightness distribution and estimate the scattered size and orientation of the source from closure amplitude and self-calibration analysis, obtaining consistent results between methods and epochs. We then use the known scattering kernel to determine the intrinsic two-dimensional source size at 3.5 mm: $(147 \pm 7 \, \mu \text{as}) \times (120 \pm 12 \, \mu \text{as})$, at position angle $88° \pm 7°$ east of north. Finally, we detect non-zero closure phases on some baseline triangles, but we show that these are consistent with being introduced by refractive scattering in the interstellar medium and do not require intrinsic source asymmetry to explain.

Key words: accretion, accretion disks – galaxies: active – galaxies: individual (Sgr A*) – Galaxy: center – techniques: interferometric

1. INTRODUCTION

The compact radio source Sagittarius A* (Sgr A*) at the center of the Galaxy is associated with a supermassive black hole of $\sim 4 \times 10^6 \, M_\odot$ (Ghez et al. 2008; Gillessen et al. 2009). The mechanism responsible for the radio emission is thought to be synchrotron from a jet-like outflow (Markoff et al. 2007; Falcke et al. 2009), a radiatively inefficient accretion flow (RIAF) onto the black hole (e.g., Narayan et al. 1995; Yuan et al. 2003; Broderick et al. 2009), or an almost isothermal jet coupled to an accretion flow (Mościbrodzka & Falcke 2013). Different jet and accretion disk models can be tested by modeling the radio through the submillimeter spectrum of Sgr A* (e.g., Markoff et al. 2007), the frequency-dependent source size (e.g., Bower et al. 2004; Mościbrodzka & Falcke 2013; Chan et al. 2015), and data from millimeter Very Long Baseline Interferometry (VLBI) observations (Broderick et al. 2011; Dexter et al. 2012).

At wavelengths longer than a few centimeters, the image of Sgr A* is heavily scattered by the intervening ionized interstellar medium, and the scattering determines the size of the measured image. The effect of this scattering decreases at shorter wavelengths, with a λ^2 dependence, and VLBI observations at wavelengths shorter than a centimeter have found deviations from the λ^2 law, suggesting that intrinsic source structure contributes to the apparent image at these wavelengths (Doeleman et al. 2001; Bower et al. 2004, 2006; Shen et al. 2005; Krichbaum et al. 2006). The intrinsic two-dimensional (2D) source size can then be estimated by extrapolating the scattering properties from longer wavelengths and then deconvolving the scattering ellipse from the observed size. At a wavelength of one millimeter or less, the scatter broadening is subdominant to intrinsic structure in the image (Doeleman et al. 2008; Fish et al. 2011; Johnson et al. 2015).

Because of the lack of good north–south baselines in existing VLBI arrays, efforts to study the intrinsic structure of Sgr A* at 3.5 mm have been mostly limited to the east–west direction. To unambiguously determine the intrinsic 2D structure of Sgr A*, VLBI observations with higher angular resolution in the north–south direction are needed. In this paper we describe such observations of Sgr A* obtained at $\lambda = 3.5$ mm with the National Radio Astronomy Observatory[10] Very Long Baseline Array (VLBA) and the Large Millimeter Telescope Alfonso Serrano (LMT) located in Central Mexico, operated in concert as a single VLBI array. This required that the LMT be equipped as a VLBI station as we now describe.

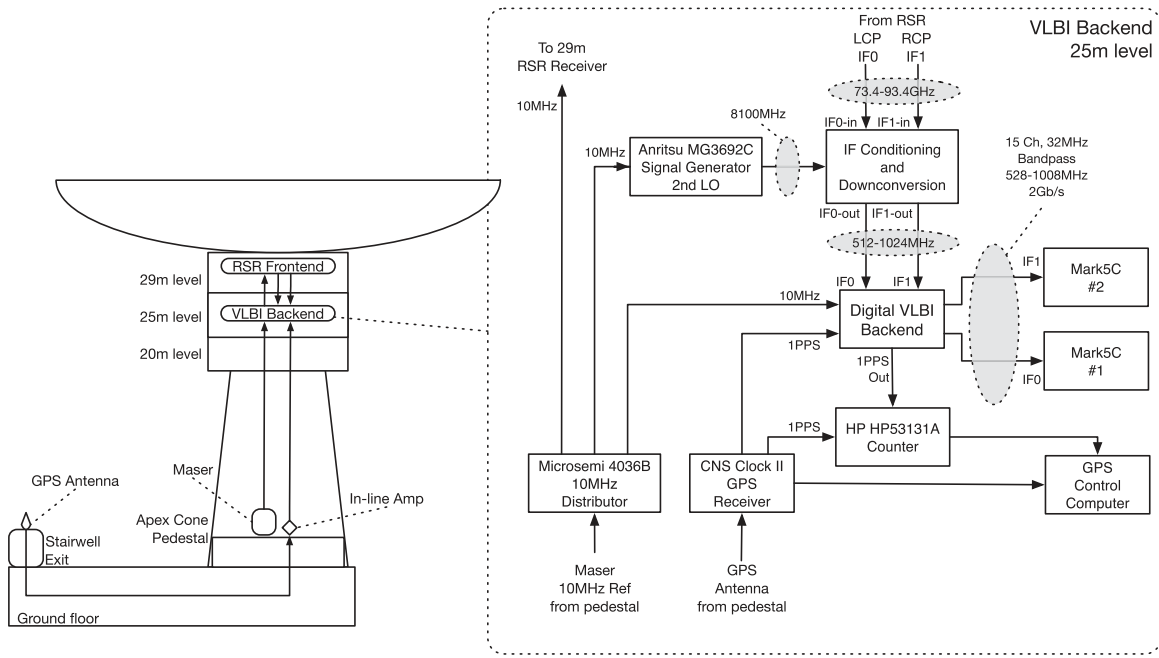[9] Consejo Nacional de Ciencia y Tecnología Research Fellow.

Figure 1. Block diagram of VLBI instrumentation setup at the LMT for the 2015 April observations.

2. VLBI AT THE LMT

Situated at an altitude of 4600 m at the summit of Volcán Sierra Negra in Central Mexico, the LMT has a large collecting area (32 m circular aperture currently operational, extending to the full 50 m diameter by 2017) and geographical location that make it particularly useful for mm-wavelength VLBI observations. Technical work leading to development of VLBI capability at the LMT was the product of a multi-year collaboration between Instituto Nacional de Astrofísica, Óptica y Electrónica, the University of Massachusetts, the Smithsonian Astrophysical Observatory, the Massachusetts Institute of Technology Haystack Observatory, the Universidad Nacional Autónoma de México (UNAM), and the NRAO. Recognizing the importance of LMT participation in 3.5 mm VLBI networks (e.g., the VLBA or the Global Millimeter VLBI Array—GMVA) and in the Event Horizon Telescope (EHT) project at 1.3 mm wavelength, these groups began planning VLBI tests in 2012. First 3.5 mm observations were scheduled in 2013 April, for which a full VLBI recording system was installed. This included integration at the Sierra Negra site of

1. a GPS receiver (model CNS) to enable synchronization with other VLBI sites;
2. a custom-built radio frequency downconverter to shift the output of the facility Redshift Search Receiver (RSR) to a standard VLBI intermediate frequency (IF) range of 512-1024 MHz;
3. a digital backend to digitize and format data for VLBI recording (Whitney et al. 2013); and
4. two high-speed hard-disk Mark5c VLBI recorders.[11]

The RSR is one of the two instruments currently available at the LMT. The RSR has two H and V linear polarization receivers that instantaneously cover a wide frequency range of

73–111 GHz and has a dedicated backend spectrometer that covers the entire band with a spectral resolution of 31 MHz (Erickson et al. 2007). The receivers are chopped between the ON and OFF source positions (beam 1 and 0, respectively) separated by 76″. Sources are tracked on beam 1 during VLBI observations. The RSR has two fixed first local oscillators at 93.4 and 112.3 GHz, which are used to downconvert the frontend band into two 0–20 GHz IF bands. For this VLBI experiment we used the 73–93.4 GHz band (see Figure 1) for further down-conversion and processing.

A hydrogen maser, typically used to provide a stable frequency reference for VLBI, was not available for the 2013 observations, so an ultra-stable quartz crystal oscillator loaned by the Applied Physics Laboratories of Johns Hopkins University was used. This unit has an Allan Deviation of $<10^{-13}$ over integration times from 1 to 10 s, resulting in coherence losses of $<25\%$ at 3.5 mm wavelength. This crystal was thus sufficient for initial tests but not for scientific observations. To convert the Linear Polarization natively received by the RSR to Circular Polarization, a quarter-wave plate made of grooved dielectric was inserted into the telescope optics, and for subsequent observations Left Circular Polarization was selected.

Using this test setup (see Figure 1), several SiO maser sources ($v = 1, J = 2 - 1$) and bright active galactic nucleus were detected on baselines from the LMT to the VLBA, confirming the stability of the LMT RSR and VLBI system performance. In 2014, this same setup was augmented by the installation and integration of a hydrogen maser frequency standard (manufactured by Microsemi), which is housed in the pedestal room of the telescope. A custom-built enclosure provides a temperature stable environment for the maser and a low-noise distribution system installed near the VLBI equipment routes the maser reference to phase lock all VLBI instrumentation.

Commissioning observations in 2014 were conducted over the course of four nights between the VLBA and the LMT. A precise

---

[11] http://www.haystack.edu/tech/vlbi/mark5/mark5_memos/057.pdf.
Unlike nominal operations of the VLBA, the LMT did not record dual polarization on the same disk set.
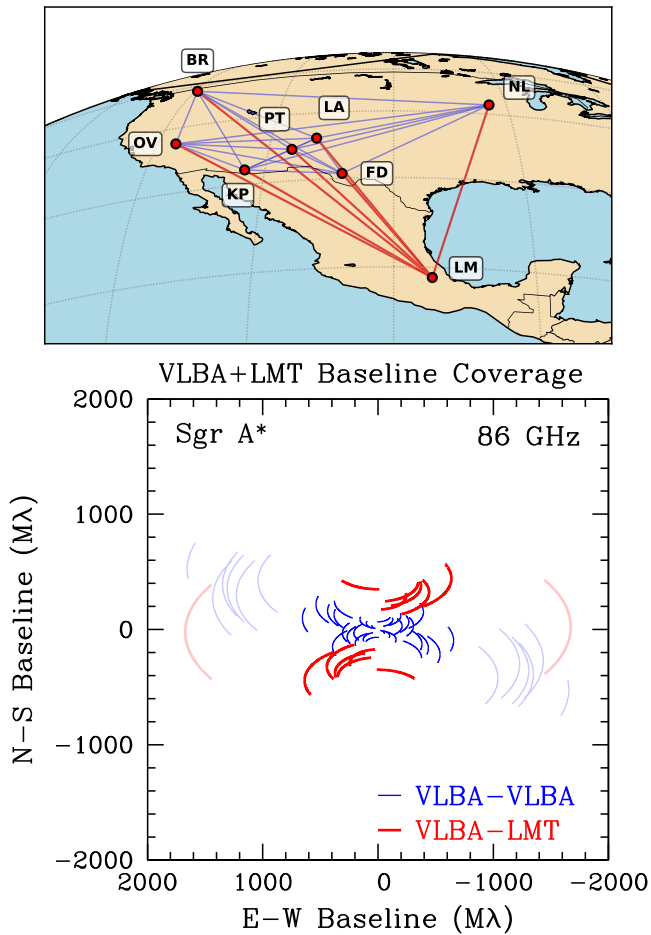
Figure 2. Top: the 3.5 mm stations of the VLBA and the LMT. Bottom: the corresponding *u*–*v* coverage; the faint tracks denote baselines to Mauna Kea, on which we do not detect Sgr A*.

position for the LMT was measured by modeling the delays and rates of VLBI detections on strong quasars over a wide range of elevation. The operational location of the LMT in the International Terrestrial Reference Frame geocentric coordinates is $(X, Y, Z) = (-7.687156(2) \times 10^5 \text{ m}, -5.9885071(2) \times 10^6 \text{ m}, 2.0633549(5) \times 10^6 \text{ m})$. This location corresponds to the projection point of the horizontal axis onto the vertical axis. Figure 2 shows the VLBA and LMT as seen by Sgr A* and the corresponding baseline coverage.

3. OBSERVATIONS AND DATA CALIBRATION

The observations reported here (project code BD183) were obtained in 2015 by operating the eight VLBA antennas equipped with 3.5 mm receivers and the LMT as a single VLBI array. The central frequency was 86.068 GHz. A total of 27 hr of telescope time were allocated to the project, which were covered in three epochs of 9 hr each on 2015 April 24, 27, and 28 (codes A, C, and D, respectively). Because scans for pointing and calibration were also included in each observation, only about 3.6 hr were actually spent on-source in each epoch. Observations were triggered at all sites based on expected weather conditions at LMT and North Liberty, the key stations of the project. Data were recorded at a rate of 2 Gb s^{-1} and taken in left circular polarization, with 480 MHz of bandwidth covered by 15 32 MHz IF channels.

In the first epoch, the LMT RSR tracked on the wrong beam (beam 0) and this was caught just before finalizing observations. On the second epoch, the station at Pie Town (PT) experienced precipitation during most of the observing run, so data were highly affected. On the third epoch, the Los Alamos (LA) recording system corrupted the data due to timing issues. Thus, the data taken at the LMT on first epoch, at PT on the second epoch, and at LA on the third epoch were discarded. Because the longest VLBI baselines between Mauna Kea and the rest of the array resolve out the emission from Sgr A*, the source was not detected on these baselines. Fringe detections on Sgr A* were therefore obtained with an array consisting of seven stations in the North American continent in each of the three epochs.

For the remainder of the paper we will focus on the last two epochs (BD183C and BD183D) because our goal of constraining the intrinsic size of Sgr A* at 3 mm relies heavily on the north–south baselines provided by the LMT.

The initial data reduction was done using the Astronomical Image Processing System (AIPS; Greisen 2003). Phase calibration was performed as follows. Corrections for the antenna axis offset at the LMT and for voltage offsets in the samplers at all stations were first applied to the data. Single-band delays were determined by fringe-fitting on a strong calibrator (3C279 for BD183C and 3C454.3 for BD183D) and the solutions were applied to all scans in the corresponding observing night. Sgr A* was then fringe-fitted, producing rate and delay solutions every 1 minute. These solutions were smoothed using a median window filter smoothing function with a six-minute filter time and then applied to the data. A single bandpass solution was derived from the autocorrelations on the continuum sources and applied to the data after fringe-fitting. At this point, all scans with non-detections were flagged. Also, the outer 4.5 MHz from the edge of each IF were discarded because these are adversely affected by the bandpass response function.

To optimize the coherent averaging of visibilities, we estimated the atmospheric coherence time of our data by examining the ratios of debiased coherent to incoherent averages[12] as a function of time using a scan on 3C279. For every baseline we found that the fractional amplitude loss is $<0.7\%$ for $t_{\text{avg}} = 10$ s (see Figure 3). Considering the fractional amplitude loss scales with the line of sight optical depth and because Sgr A* is at lower elevation, we estimated the loss increases to $<4\%$ in the worst case. To ensure that closure relationships (discussed below) were not affected by coherence losses, we then utilized 10 s coherent averages. For this segment of time, the losses can be considered negligible in all of our data. After this coherent averaging in time and across the full bandwidth, these phase-only calibrated data were exported as FITS files for further analysis outside of AIPS.

4. ANALYSIS

VLBI visibilities were analyzed via two standard pathways: the first analysis used only "closure" quantities, which provide immunity to station-based calibration errors, and the second

---

[12] A coherent average takes the vector-average of complex visibilities, preserving the coherence of phase over time and frequency (Thompson et al. 2007). An incoherent average takes the scalar-average of complex visibilities segmented at short-length times. A debiased average corrects visibility amplitudes by the noise bias introduced because of the inherently positive nature of amplitudes.
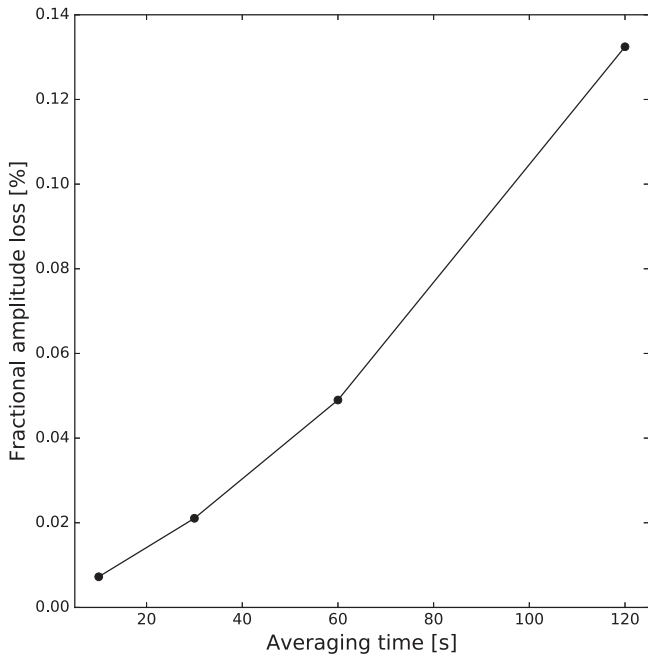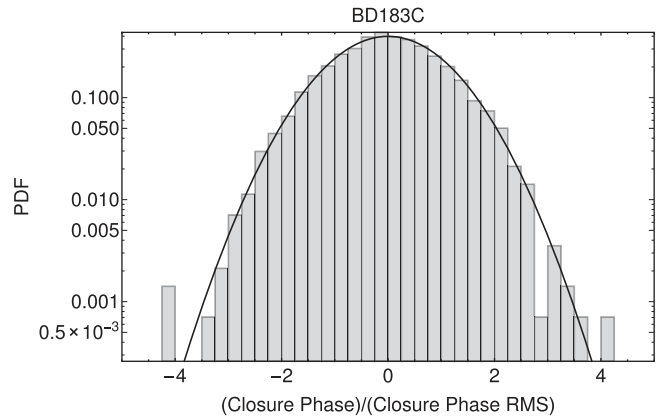
Figure 3. Fractional amplitude loss as a function of averaging time for a scan on 3C279 taken in the first epoch. We estimated this fraction for each baseline and took the maximum values to show in the plot.

Figure 4. Probability density function (PDF) of the standardized closure phases on all triangles with baselines shorter than $250 \, M\lambda$. The solid line shows a fitted Gaussian, representing zero intrinsic closure phase and non-zero measurements entirely due to thermal noise. We use this Gaussian fit to estimate the scaling factor relating each "weight" reported by AIPS for a complex visibility to the thermal noise.

analysis used "self-calibration," which attempts to simultaneously solve for source structure and complex, time-dependent station gains.

4.1. Fitting an Elliptical Gaussian Using Closure Amplitudes

For a closed triangle of interferometric baselines, the phase of the bispectrum (the directed product $V_{12} V_{23} V_{31}$ of the three complex visibilities V_{ij} around the triangle) is immune to any station-based phase errors. This quantity is known as a "closure phase." Likewise, closure amplitudes, such as $|(V_{12} V_{34})/(V_{13} V_{24})|$, can be constructed for any quadrangle of sites and provide immunity to station-based gain amplitude errors (Thompson et al. 2007). We constructed closure amplitudes and phases from the phase-only calibrated data for each 10 s time segment.

Measured closure phases from both days are consistent with a zero-mean Gaussian distribution (see Figure 4). We then fit the distribution of closure phases to calculate a single coefficient that converts AIPS weights w_i to thermal noise $\sigma_i \propto 1/\sqrt{w_i}$ for each measurement. Because the atmospheric coherence time at $\lambda = 3.5$ mm is only tens of seconds and because coherent averages must be done over even shorter timescales to preserve the closure relationships discussed below, most of our measurements have only moderate signal-to-noise. For example, the median signal-to-noise ratio (S/N) in our two observing epochs was 8.3 and 7.2, respectively, for all detections, but ~10% of detections have S/N < 3. Both closure amplitudes and phases have markedly non-Gaussian errors in this regime, and closure amplitudes suffer a noise bias. For example, for a closure amplitude constructed from four visibilities that each have an S/N of 3, the average will be biased upward by 30%, and estimates of the closure amplitude uncertainty using high-S/N properties will be incorrect. For this reason, we derived the conversion between AIPS weights and thermal noise using closure phases with S/N > 3, and we

used Monte Carlo simulations to estimate the bias and uncertainties in our closure quantities.

Even after averaging our closure phases over each epoch, they are still close to zero, which is consistent with an elliptical Gaussian structure. Consequently, for both epochs BD183C and BD183D, we performed a least-squares fit of elliptical Gaussian source models to the closure amplitudes (see Figure 5). To avoid errors that were significantly non-Gaussian and the associated bias, we only used closure amplitudes constructed from visibilities that had S/N > 3 in their 10 s coherent average for these fits.

The best-fit solutions have a reduced χ^2 of 1.50 for BD183C and 1.25 for BD183D. These values are greater than unity at high significance, so to determine whether the excess can be entirely accounted for by the non-Gaussian closure amplitude errors we generated synthetic data sets for each epoch using the best-fit elliptical Gaussian model for the source. We sampled the model on each baseline for which there was a detection and added the expected amount of thermal noise to each sample. Finally, we calculated closure amplitudes for these synthetic data and used them to find the best-fit elliptical Gaussian. This procedure successfully reproduced the input model within the derived uncertainties and found a corresponding reduced χ^2 of ~1.25 in both epochs. Thus, the excess in our reduced χ^2 is comparable to what is expected from the non-Gaussian errors on the closure amplitudes.

Unlike previous efforts (e.g., Bower et al. 2004, 2014b; Shen et al. 2005), we did not use the χ^2 hypersurface to estimate parameter uncertainties in the fits to closure amplitudes. Several problems in this approach have been noted by Doeleman et al. (2001). Namely, because the closure amplitudes are not independent, a fixed increase $\Delta\chi^2$ does not accurately represent an expected confidence interval. As a trivial example of this, duplicating a data set will double the $\Delta\chi^2$ but obviously does not constrain model parameters better. Because there are nominally ~N^4 closure amplitudes for N stations but only ~N^2 visibilities and independent closure amplitudes, the redundant information can be substantial. Non-Gaussian noise, especially the high tail in the closure amplitude distribution, can also invalidate a standard χ^2 approach.
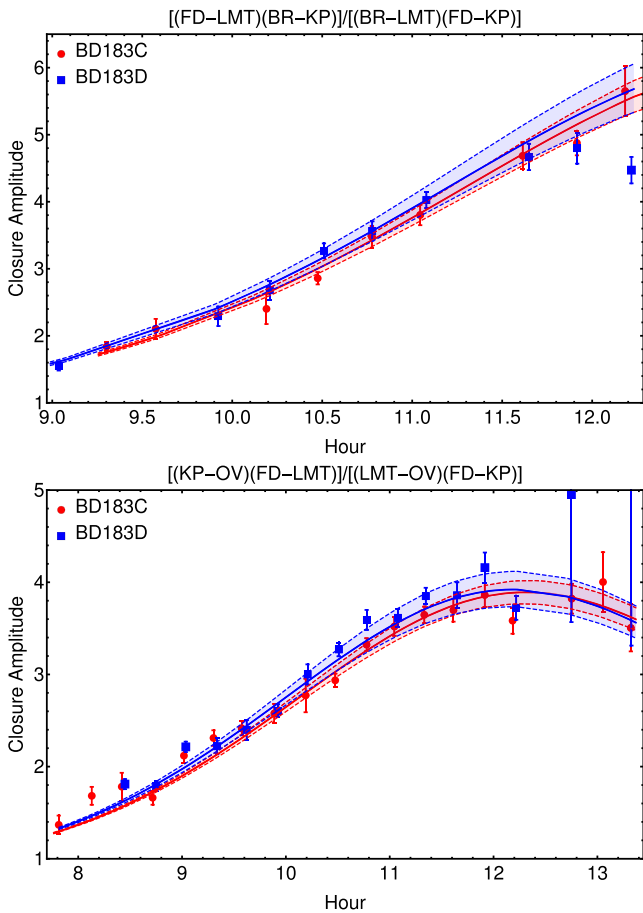
Figure 5. Examples of closure amplitudes on two quadrangles. The points show scan-averaged closure amplitudes. The lines and shaded regions show the best-fit model from self-calibration in each epoch and $\pm 1\sigma$ uncertainty.

Instead, we estimated the uncertainty of the Gaussian parameters using a Monte Carlo simulation, independently fitting elliptical Gaussians to 20 different new data sets that each added additional thermal noise to the original complex visibilities with equal standard deviation to their original thermal noise before constructing the closure amplitudes for each set. We then report uncertainties given by the scatter in the fitted parameters. Note that because this procedure decreases the S/N of each measurement by a factor of $1/\sqrt{2}$, it conservatively estimates the parameter uncertainties. Table 1 gives our best-fit model and its associated uncertainty in each epoch.

4.2. Fitting an Elliptical Gaussian Using Self-calibration

We also fit an elliptical Gaussian to the complex visibilities using "self-calibration." This approach fits the Gaussian model simultaneously with time-dependent complex station gains. In this case, measurement uncertainties are described simply as additive complex Gaussian noise, and so there is neither bias nor non-Gaussian noise to contend with, even when the S/N is low. Thus, self-calibration can reliably utilize weaker detections than the closure-only analysis.

A concern for self-calibration is that the derived model can be heavily biased by the input self-calibration model (the initial guess for the source structure), especially if the minimization is not permitted to iteratively converge (Bower et al. 2014b

illustrates this unsurprising bias for self-calibration with a single iteration). A second concern is that parameters reported for self-calibration are often computed without accounting for the uncertainties in the self-calibration parameters—the $\Delta\chi^2$ is explored over the space of model parameters while holding the best-fit self-calibration solution constant. Such estimates can significantly underestimate model parameter uncertainties.

We self-calibrated our data by independently deriving gain solutions for every 10 s integration. We confirmed that the self-calibration (iteratively) converged to the same solution regardless of the initially specified model. Specifically, we checked convergence by comparing the results with two initial models: a point source and a 500 μas circular Gaussian source.

We then use the χ^2 hypersurface of both the self-calibration and elliptical Gaussian parameters to evaluate uncertainties in the model. We only included points with S/N > 3 to avoid potentially spurious or corrupted detections. This restriction eliminates $\approx$10% of our data but only <2% of the LMT detections because of their higher S/N. The best-fit model in each epoch and the corresponding model uncertainties are given in Table 1.

We also repeated the estimate of uncertainties in the Gaussian model parameters while holding the self-calibration solution constant and equal to the best-fit self-calibration solution (this is the most straightforward self-calibration approach in AIPS, for instance). The derived Gaussian parameter uncertainties were a factor of $\sim$6 smaller for the major and minor axes, and were a factor of $\sim$10 smaller for the position angle, showing that the self-calibration uncertainties are a critical part of the error budget even when the self-calibration is allowed to iteratively converge.

4.3. Self-calibration Versus Closure-only Analysis

There has been considerable discussion in the literature about whether self-calibration or closure-only analysis is preferable for fitting Gaussian models to Sgr A* (e.g., Doeleman et al. 2001; Bower et al. 2004, 2014b; Shen et al. 2005). We have performed both analyses and found consistent results both in the best-fit models and for their associated parameter uncertainties when the self-calibration model uncertainties are properly taken into account. We do find that the self-calibration uncertainties are still smaller by a factor of $\sim$2, even after accounting for uncertainties in the self-calibration solution. Overall, our data suggest that both approaches should be used and checked for consistent results; differences may highlight problems in the assumptions for deriving the uncertainties of either model.

4.4. The Role of the LMT

Prior attempts to constrain the minor (NS) axis size of Sgr A* have met with varied success. Shen et al. (2005), who analyzed closure amplitudes, could only determine an upper bound for the minor axis size; likewise, Lu et al. (2011), who self-calibrated to an elliptical Gaussian model, found that in 2 out of 10 observing epochs the elliptical model is under-determined. When LMT baselines are excluded from the analysis presented here, the results are similar. Specifically, even when including weak detections, self-calibration to the BD183C data without the LMT gave a minor axis size of 153 ± 15 μas. However, in BD183D, the self-calibration finds a best-fit minor axis of 67^{+40}_{-67} μas (i.e., a size of zero is

Table 1
Summary of Elliptical Gaussian Fits to 3 mm VLBI of Sgr A*

| | BD183C | | BD183D | | Doeleman+('01) | Shen+('05) | Lu+('11) |
	Closure Amp.	Self-Calibration	Closure Amp.	Self-Calibration	Self-Calibration	Closure Amp.	Self-Calibration
Major axis	$214.9 \pm 4.0\ \mu$as	$212.7 \pm 2.3\ \mu$as	$217.7 \pm 5.0\ \mu$as	$221.7 \pm 3.6\ \mu$as	$180 \pm 20\ \mu$as	$210^{+20}_{-10}\ \mu$as	$210 \pm 10\ \mu$as
Minor axis	$139.0 \pm 8.1\ \mu$as	$138.5 \pm 3.5\ \mu$as	$147.3 \pm 8.0\ \mu$as	$145.6 \pm 4.0\ \mu$as	$\cdots$	$130^{+50}_{-130}\ \mu$as	$130 \pm 10\ \mu$as
P.A.	$80°\!.8 \pm 3°\!.2$	$81°\!.1 \pm 1°\!.8$	$80°\!.2 \pm 4°\!.8$	$75°\!.2 \pm 2°\!.5$	$\cdots$	$79^{+12}_{-33}°$	$83°\!.2 \pm 1°\!.5$
Axial ratio	1.55 ± 0.08	1.54 ± 0.04	1.48 ± 0.07	1.52 ± 0.05	$\cdots$	$1.62^{+20}_{-0.6}$	1.62 ± 0.11

Note. Our elliptical Gaussian fits to the scattered image of Sgr A* at $\lambda = 3.5$ mm and previously published values. Major and minor axes are given as the FWHM. Doeleman et al. (2001) found that their data did not warrant an elliptical Gaussian model rather than a circular Gaussian; their quoted uncertainties include the effects from uncertainties in the self-calibration solution and from thermal noise. Shen et al. (2005) only placed upper limits on the minor axis and did not measure anisotropy at high statistical significance. Lu et al. (2011) reported fits and uncertainties from self-calibration and used the spread of fitted size among different epochs to estimate the overall uncertainty. However, their reported spread in fitted values from epoch to epoch did not include the two epochs for which an elliptical model is underdetermined. Consequently, the uncertainties reported by Lu et al. (2011) in minor axis size are likely too small by a factor of $\sim$2–3. Note that the axial ratio and its corresponding uncertainty was not reported in Shen et al. (2005) or Lu et al. (2011); we derived these quantities using a skew normal distribution for the Shen et al. (2005) results and a normal distribution for Lu et al. (2011), each with uncorrelated errors on the major and minor axes.

Table 2
Summary of Intrinsic Sizes of Sgr A* at 3.5 mm

| | BD183C | | BD183D | | Doeleman+('01) | Shen+('05) | Lu+('11) |
	Closure Amp.	Self-Calibration	Closure Amp.	Self-Calibration	Self-Calibration	Closure Amp.	Self-Calibration
Major axis	$145 \pm 9\ \mu$as	$142 \pm 7\ \mu$as	$149 \pm 9\ \mu$as	$155 \pm 8\ \mu$as	$82 \pm 46\ \mu$as	$136^{+32}_{-18}\ \mu$as	$139 \pm 17\ \mu$as
Minor axis	$114^{+14}_{-19}\ \mu$as	$113^{+11}_{-17}\ \mu$as	$124^{+13}_{-17}\ \mu$as	$122^{+11}_{-16}\ \mu$as	$\cdots$	$104^{+65}_{-164}\ \mu$as	$102 \pm 21\ \mu$as
P.A.	$88°^{+9}_{-4}$	$89°^{+10}_{-4}$	$87°^{+13}_{-4}$	$69°^{+3}_{-5}$	$\cdots$	$82^{+15}_{-34}°$	$95° \pm 10°$
Axial ratio	$1.27^{+0.26}_{-0.15}$	$1.25^{+0.22}_{-0.12}$	$1.20^{+0.21}_{-0.12}$	$1.27^{+0.19}_{-0.12}$	$\cdots$	$1.31^{+0.87}_{-2.07}$	1.36 ± 0.33

Note. We apply the same deconvolution scheme to the measured sizes by Doeleman et al. (2008), Shen et al. (2005), and Lu et al. (2011) to arrive at the values listed in this table. Notice that the measurement by Lu et al. (2011) resulted from an average over eight epochs, while here we are able to determine the intrinsic size and orientation at individual epochs.

excluded at a significance of $<1\sigma$). Likewise, in both epochs, fits using only closure amplitudes could only estimate an upper bound for the minor axis size, so the self-calibration solutions must be interpreted with caution. We then conclude that past measurements could only confidently measure an upper bound for the minor axis size of the scattered image of Sgr A* at $\lambda = 3.5$ mm in individual observing epochs. This analysis confirms that inclusion of the LMT baselines is essential to the robust determination of the intrinsic size in the north–south direction. This result is unsurprising because the geographical location and size of the LMT significantly improves the north–south coverage and sensitivity of the VLBI array.

5. THE INTRINSIC SIZE OF SGR A*

The size of the scattering ellipse can be estimated based on the wavelength-dependent size of Sgr A* at wavelengths longer than a few cm. Bower et al. (2006) determined the normalization of the scattering law to be given according to 1.31×0.64 mas cm^{-2} at 78° east of north. The uncertainties in these values are ± 0.03 mas in major axis size, $+0.04$ and -0.05 mas in minor axis size and $\pm 1°$ in position angle. At 3.5 mm, this law gives scattering sizes of $159.2 \pm 3.6\ \mu$as and $77.8^{+4.9}_{-6.1}\ \mu$as for major and minor axis, respectively. This ellipse is smaller that the ellipse measured at both epochs from closure quantities and self-calibration, which means that we are detecting the intrinsic structure of the source. However, Psaltis et al. (2015) have also analyzed the set of measured sizes of Sgr A* and suggest that there are large systematic errors in the minor axis size. Indeed, our comparison of self-calibration and

closure-only results reinforces the suspicion that uncertainties derived in previous experiments may be systematically low.

We deconvolve the measured ellipse with the scattering ellipse to determine the intrinsic size and orientation of Sgr A*. To properly account for the errors, we perform a Monte Carlo simulation. For this simulation we create 10,000 realizations of the observed ellipse by taking independently a major axis size, a minor axis size, and a position angle from Gaussian distributions with standard deviations equal to the errors given in Table 1. For each of these realizations we similarly create a realization of the scattering ellipse, with parameters taken from Gaussian distributions that have a variance equal to the quadratic sum of the errors reported by Bower et al. (2006) and the systematic errors by Psaltis et al. (2015). These systematic errors are 3% in the major axis, 25% in the minor axis, and 12% in the position angle. We then take the deconvolution with the observed ellipse for each realization and compute the ratio of major to minor axis, $A_{\rm int}$. The resulting distributions are symmetric Gaussians for the intrinsic major axes with means and standard deviations given in Table 2. The distributions for minor axis, position angle, and axial ratio are non-Gaussian, so we give for those the median and the 15.87th and 84.13th percentiles ($-\sigma$ and $+\sigma$) in Table 2. We note that errors estimated using this approach are comparable to those derived by standard error propagation. Within the accuracy of our measurements, we do not see significant variations from one epoch to other in the intrinsic sizes of major and minor axis, and in position angle. For our two observations, we performed a weighted average of the closure and self-calibrated intrinsic size estimates to arrive at an intrinsic ellipse of $147 \pm 6\ \mu$as $\times\ 120^{+10}_{-13}\ \mu$as, at $88°^{+7}_{-3}$ for the
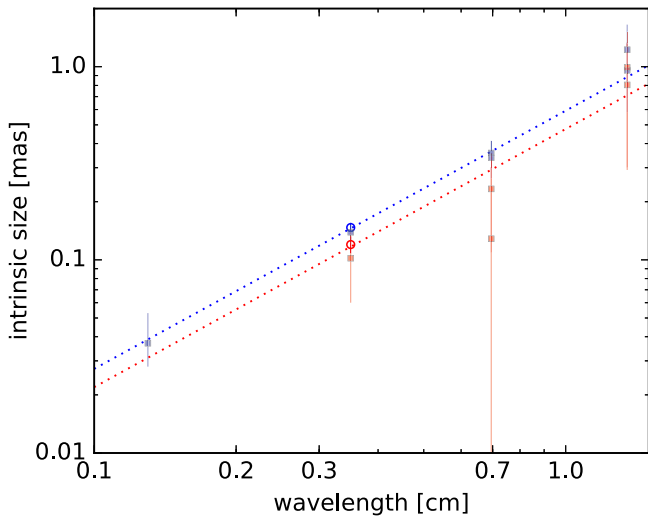
Figure 6. Plot of intrinsic major (blue) and minor (red) axis size vs. wavelength. The open circles at 3.5 mm correspond to the measurements reported in this work from closure approach. The squares at 1.3, 3.5, 7, and 13.5 mm were obtained by reanalyzing the measurements from Doeleman et al. (2008), Bower et al. (2004, 2014b), and Lu et al. (2011). The dotted lines represent a fit to a power-law trend with common index of 1.34 ± 0.13 for both major and minor axes.

closure approach and $148 \pm 5\ \mu$as $\times\ 118^{+8}_{-10}\ \mu$as, at $81° \pm 3°$ for the self-calibration approach. The corresponding axial ratios of major to minor intrinsic size are $1.23^{+0.16}_{-0.09}$ and $1.26^{+0.14}_{-0.08}$, respectively. Considering that the Schwarzschild radius (R_{sch}) for a black hole of mass $4.3 \times 10^6\ M_\odot$ (Gillessen et al. 2009) at a distance of 8.34 kpc (Reid et al. 2014) is 10.2 μas, the intrinsic angular sizes can be translated into physical sizes. The resulting values are $14.4 \pm 0.6\ R_{\mathrm{sch}} \times 11.8^{+1.0}_{-1.3}\ R_{\mathrm{sch}}$ for the closure approach and $14.5 \pm 0.5\ R_{\mathrm{sch}} \times 11.6^{+0.8}_{-1.0}\ R_{\mathrm{sch}}$ for the self-calibration approach.

We now use past measurements of the scattered image at 1.3, 7, and 13.5 mm to study the dependence of the intrinsic size as a function of wavelength. We again use the kernel from Bower et al. (2006) to remove the effects of scattering and determine the intrinsic size of major and minor axis at these wavelengths.

At 7 mm, the scattered 2D image has been reported by Bower et al. (2014b), Lu et al. (2011), and Shen et al. (2005). At 13.5 mm, there are measurements by Bower et al. (2004) and Lu et al. (2011). We follow the approach described above for deconvolution of these five size measurements with the scattering ellipse. At 1.3 mm, the (NS) apparent size is not well-constrained (Doeleman et al. 2008), so the scattered source at this wavelength is assumed to be given by a circular Gaussian distribution. We find that intrinsic sizes at a given wavelength from measurements by different authors are consistent within the errors.

We note that when the uncertainties reported by Psaltis et al. (2015) are included in the error budget of the scattering kernel, the axial ratio of intrinsic sizes at 7 mm is not statistically significant. Specifically, an axial ratio of $2.78^{+4.79}_{-4.94}$ is found and then this measurement should be treated with caution.

To investigate if the axial ratio scales with wavelength, we show in Figure 6 the intrinsic sizes derived from the measurements by Doeleman et al. (2008) at 1.3 mm, Bower et al. (2014b) at 7 mm, Bower et al. (2004) at 13.5 mm, as well as the measurements from Lu et al. (2011) at 3.5, 7 and 13.5 mm, where we have multiplied the minor axis uncertainty

at 3.5 mm by a factor of two. Our weighted averages of sizes derived from the closure approach at 3.5 mm using the new observations presented here are also shown as open circles.

Assuming that the data can be represented by a λ^β law, we performed a weighted least-squares linear fit to all measurements obtaining $\beta = 1.34 \pm 0.13$. If the power-law indices for the major and minor axes are allowed to differ, the respective fits give $\beta = 1.35 \pm 0.14$ and $\beta = 1.26 \pm 0.38$. The errors in the power-law indices are taken from the diagonal entries of the covariance matrix constructed for the fits. Hence, within the errors of the measurements, the intrinsic size of the major and minor axes follow the same power law. More precise measurements at wavelengths other than 3.5 mm are necessary to enable a robust fit from the minor axis data alone and an investigation of the dependence of the intrinsic shape on wavelength.

The observed size at 3.5 mm also gives an absolute upper limit on the scatter broadening along the minor axis. Our measurements at both epochs are only 1.4–1.7σ above the minor axis suggested by Psaltis et al. (2015) at 3.5 mm, significantly constraining the scattering kernel.

6. DISCUSSION

6.1. Effects from Refractive Scattering

The "blurring" from interstellar scattering that causes the λ^2 scaling of the scattered image of Sgr A* at wavelengths longer than a few centimeters is an ensemble-average effect and so only strictly applies when the scattered image is averaged over a long period of time. Diffractive scattering of the intrinsic image with an elliptical Gaussian kernel does not affect closure phase (Fish et al. 2014). However, within individual observing epochs, refractive scattering causes the image to become fragmented and it does introduce stochastic non-zero closure phase variations (Johnson & Gwinn 2015). The imprint of these stochastic fluctuations can then be used to constrain properties of both the intrinsic source and the turbulence in the scattering material (Gwinn et al. 2014).

Refractive scattering causes flux modulation and positional variation (image wander) at scales smaller than the scattered size (Rickett et al. 1984; Blandford & Narayan 1985; Cordes et al. 1986; Narayan 1992). On baselines that are long enough to resolve the ensemble-average image, the refractive scattering introduces small-scale power from substructure that affects interferometric visibilities and which can be estimated analytically (Goodman & Narayan 1989; Narayan & Goodman 1989; Johnson & Gwinn 2015). However, effects from refractive scattering on closure amplitudes and closure phases for baselines that weakly or moderately resolve the image are difficult to estimate analytically. For this reason, we use numerical simulations of the refractive scattering to estimate the expected effects on our measurements.

Following the methodology outlined in Johnson & Gwinn (2015), we generated an ensemble of 500 scattered images of a circular Gaussian source with an intrinsic FWHM of 130 μas. For each image, we generated a scattering screen with $2^{13} \times 2^{13}$ correlated random phases corresponding to a Kolmogorov spectrum for the turbulence and we determined the strength of the scattering by extrapolating the frequency-dependent angular size from longer wavelength measurements (Bower et al. 2006). We assumed a scattering screen, placed at a distance of 5.8 kpc from the Galactic Center, as inferred by the
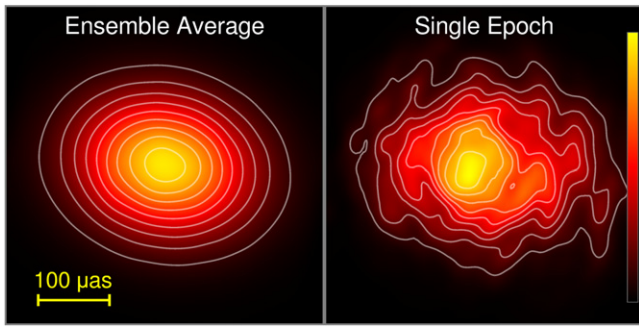
Figure 7. Simulated scattered images of Sgr A* at $\lambda = 3.5$ mm; color denotes brightness on a linear scale, shown at the far right and image contours are 10% to 90% of the peak brightness, in steps of 10%. The intrinsic source is modeled as a circular Gaussian with a FWHM of 130 μas; the ensemble-average scattered image has a FWHM of (206 μas) × (151 μas). The left image shows an approximation of the ensemble-average image, obtained by averaging 500 different scattering realizations. This image illustrates the "blurring" effects of scattering when averaged over time. The right image shows the appearance for a single epoch, which exhibits scattering-induced asymmetries that would persist over a characteristic timescale of approximately one week. Each image has been convolved with a 20 μas restoring beam to emphasize the features that are potentially detectable at $\lambda = 3.5$ mm.

combination of angular and temporal broadening from the Galactic Center magnetar (Bower et al. 2014a; Spitler et al. 2014). Refractive effects are, however, rather insensitive to the placement of the screen, with their strength scaling with $D^{-1/6}$, where D is the observer–screen distance (Johnson & Gwinn 2015). Figure 7 shows an example image from these scattering simulations.

Each screen phase "pixel" had a linear dimension of approximately 0.5 μas corresponding to 2×10^5 km, which is still insufficient to resolve the phase coherence length, r_0, of the scattering screen, which is (1200 km) × (2400 km) as determined by the angular size, θ_{scatt} of the scattering kernel ($r_0 \sim \lambda/\theta_{scatt}$). Because of this limitation, we set the inner scale, r_{in}, of the scattering to be equal to the pixel resolution to ensure that the unresolved phase variations were smooth. For this reason, our simulations have slightly more refractive noise than expected, by a factor of $\approx (r_{in}/r_0)^{1/6} \sim 1.6$, where r_0 is the phase coherence length of the scattering along the major axis. We divide the fluctuations of our simulations by this correction factor to derive comparisons with data.

Our simulations gave a root mean square flux modulation of 6.6%, which is reasonably close to the result from analytic calculations of 5.6%. They also predict fractional modulation of the major and minor axes of the measured image of 3.1% and 1.5%, respectively, or about 7 μas for the major axis and 2 μas for the minor axis. The expected fluctuation in the position angle of the scattered image is 2°.0. These fluctuations are potentially detectable among a set of multiple epochs when the LMT participates in VLBI with the VLBA. However, because our two observing epochs with the LMT are on consecutive days and the scattering likely evolves on a timescale of a week, the inter-epoch consistency in our measured parameters (see Table 1) is expected. The timescale for the stochastic fluctuations to evolve is approximately given by the transverse size of the scatter-broadened image at the location of the scattering material divided by the transverse velocity of the scattering material (Johnson & Gwinn 2015). Assuming a transverse velocity of 50 km s^{-1}, we derive a characteristic timescale of approximately two weeks for the refractive scattering to evolve.

The fluctuations in visibility phase on each baseline are primarily determined by the visibility amplitude on that baseline. For an ensemble-average normalized visibility amplitude of $0.1 \lesssim |V| \lesssim 0.5$, the phase fluctuations in our numerical simulations are approximately $0.05/|V|$ (radians) for long east–west baselines and $0.03/|V|$ (radians) for long north–south baselines. However, because the phase fluctuations are correlated on similar baselines, the closure phase fluctuations are not well-approximated by the quadrature sum of these fluctuations. For example, phase fluctuations from image wander are entirely canceled in closure phase.
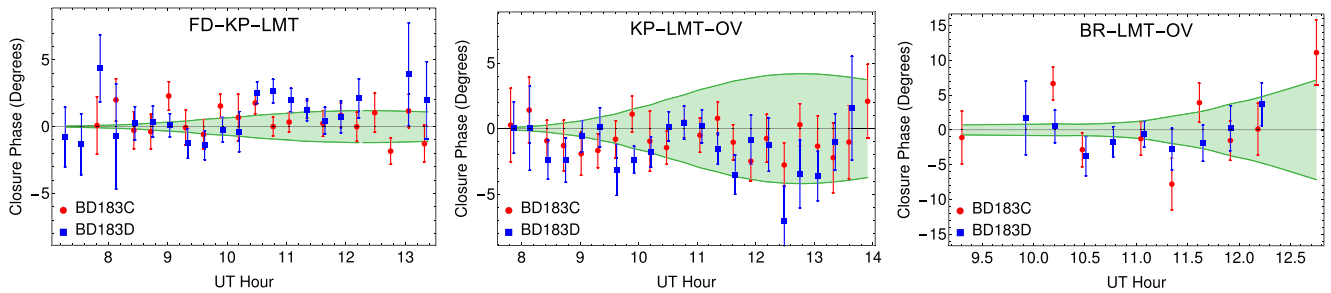
Figure 8 compares our measured closure phases as a function of time on three representative baseline triangles with the root mean square fluctuations expected from refractive scattering. Our data exhibit some non-zero closure phases at high statistical significance ($\gtrsim 4\sigma$), but these values are consistent with being introduced by the scattering. Thus, while we find evidence for non-zero closure phases, we do not find evidence for intrinsic non-zero closure phases. With additional observing epochs, the level of closure phase fluctuations could be used to constrain the scattering kernel and intrinsic structure of Sgr A* without relying on extrapolating the scattering kernel from longer wavelengths.

6.2. Constraints on the Stratified Emission Structure of Sgr A*

Our measurement of intrinsic source size at 3.5 mm and the λ^β intrinsic size scaling provides a crucial constraint for any model of the emission from Sgr A*. Models that successfully reproduce the radio properties of Sgr A* usually separate outflow from accretion inflow for the emission. On the one hand, RIAF models (e.g., Yuan et al. 2003; Broderick et al. 2009) suggest that the submillimeter emission stems from thermal electrons in the inner parts of the accretion flow. The intrinsic intensity profile, however, cannot be well described by a Gaussian distribution (Yuan et al. 2006). In the semi analytical jet model of Falcke & Markoff (2000), on the other hand, the intrinsic structure is comprised of two components, the jet and the nozzle, whose length and width at 3.5 mm are $\sim$160 μas (15.7 R_{sch}) and $\sim$48 μas (4.7 R_{sch}), respectively. At this frequency the nozzle dominates the millimeter emission. In this model the jet length scales as λ^m, with $m \sim 1$, and the axial ratio of major to minor axis of the jet is $\sim$3 at 3.5 mm. While our results support a power-law dependence of the intrinsic size close to 1, we have found a somewhat symmetric deconvolved size, which does not agree with the intrinsic anisotropic structure predicted by such jet model.

More sophisticated models in which jets are coupled to a RIAF, are equally successful in explaining the spectrum of Sgr A*. Mościbrodzka et al. (2014) conclude that the radio appearance is dominated by the outflowing plasma; however, the geometry of the emitting region depends on model parameters such as electron temperature in the jet and accretion disk, the inclination angle of the jet, and the position angle of the black hole spin axis. Nevertheless, their best (bright jet) models are within the size constraint imposed by our measurements at 3.5 mm.

To unambiguously distinguish between the various models more accurate closure phase measurements are needed. In addition, multi-epoch observations will be essential to unambiguously distinguish between intrinsic structure and refractive substructure from interstellar scattering. The LMT has recently joined the EHT for 1.3 mm VLBI observations of

Figure 8. Measured closure phases in each observing epoch as a function of time on three representative baseline triangles. The $\pm 1\sigma$ range of closure phase expected from refractive scattering of a 130 μas circular Gaussian source is shown as the green shaded region of each plot. When the two epochs are combined, the average closure phases of the FD-KP-LMT ($0^\circ\!.67 \pm 0^\circ\!.17$) and KP-LMT-OV ($-1^\circ\!.02 \pm 0^\circ\!.24$) triangles are each non-zero at a significance of $\sim 4\sigma$. However, these values are consistent with the expected closure phase excursions introduced by refractive scattering. Note that the scattering-introduced closure phases are largest when the visibility amplitudes are smallest, so the largest non-zero closure phases are also the most difficult to detect.

Sgr A* and ALMA is planned to do so in the near term. Because at 1.3 mm the source structure is less contaminated by scattering, the EHT (Doeleman et al. 2009) operating in its full configuration will enable image reconstruction of Sgr A*, and the first direct images of this nearest supermassive black hole.

7. SUMMARY

We have used VLBI to study Sgr A* at 3.5 mm wavelength. Our results are the first to use the LMT as part of a VLBI network, providing significant improvements to the VLBA, especially in the north–south array coverage. We find that the image of Sgr A* at this wavelength is well characterized as an elliptical Gaussian and we determine a robust measurement of the intrinsic size at this wavelength separately in two observing epochs. When our data are analyzed without including the LMT, we are unable to meaningfully constrain the intrinsic north–south structure because the LMT adds the critical north–south baseline coverage. We also find that previous experiments reported significantly underestimated uncertainties in the minor axis size, principally because they did not consider the systematic errors in the scattering kernel. Our data show non-zero closure phases in Sgr A*, but we demonstrate that these values are consistent with being introduced by refractive scattering in the ionized interstellar medium; they do not yet provide evidence for asymmetric intrinsic structure at 3.5 mm wavelength. Our measurements provide guidance for simulations and theories that describe the energetic accretion and outflow from Sgr A* and they highlight the importance of refractive interstellar scattering for understanding the intrinsic structure of Sgr A* with short-wavelength VLBI imaging.

Facilities: VLBA, LMT.

REFERENCES

Blandford, R., & Narayan, R. 1985, MNRAS, 213, 591
Bower, G. C., Deller, A., Demorest, P., et al. 2014a, ApJL, 780, L2
Bower, G. C., Falcke, H., Herrnstein, R. M., et al. 2004, Sci, 304, 704
Bower, G. C., Goss, W. M., Falcke, H., Backer, D. C., & Lithwick, Y. 2006, ApJL, 648, L127
Bower, G. C., Markoff, S., Brunthaler, A., et al. 2014b, ApJ, 790, 1
Broderick, A. E., Fish, V. L., Doeleman, S. S., & Loeb, A. 2009, ApJ, 697, 45
Broderick, A. E., Fish, V. L., Doeleman, S. S., & Loeb, A. 2011, ApJ, 738, 38
Chan, C.-K., Psaltis, D., Özel, F., Narayan, R., & Sadowski, A. 2015, ApJ, 799, 1
Cordes, J. M., Pidwerbetsky, A., & Lovelace, R. V. E. 1986, ApJ, 310, 737
Dexter, J., Agol, E., Fragile, P. C., & McKinney, J. C. 2012, JPhCS, 372, 012023
Doeleman, S., Agol, E., Backer, D., et al. 2009, The Astronomy and Astrophysics Decadal Survey. Science White Papers, 68
Doeleman, S. S., Shen, Z.-Q., Rogers, A. E. E., et al. 2001, AJ, 121, 2610
Doeleman, S. S., Weintroub, J., Rogers, A. E. E., et al. 2008, Natur, 455, 78
Erickson, N., Narayanan, G., Goeller, R., & Grosslein, R. 2007, in ASP Conf. Ser. 375, From Z-Machines to ALMA: (Sub)Millimeter Spectroscopy of Galaxies, ed. A. J. Baker et al. (San Francisco, CA: ASP), 71
Falcke, H., & Markoff, S. 2000, A&A, 362, 113
Falcke, H., Markoff, S., & Bower, G. C. 2009, A&A, 496, 77
Fish, V. L., Doeleman, S. S., Beaudoin, C., et al. 2011, ApJL, 727, L36
Fish, V. L., Johnson, M. D., Lu, R.-S., et al. 2014, ApJ, 795, 134
Ghez, A. M., Salim, S., Weinberg, N. N., et al. 2008, ApJ, 689, 1044
Gillessen, S., Eisenhauer, F., Trippe, S., et al. 2009, ApJ, 692, 1075
Goodman, J., & Narayan, R. 1989, MNRAS, 238, 995
Greisen, E. W. 2003, in Information Handling in Astronomy—Historical Vistas, Vol. 285, ed. A. Heck (Dordrecht: Kluwer Academic Publishers), 109
Gwinn, C. R., Kovalev, Y. Y., Johnson, M. D., & Soglasnov, V. A. 2014, ApJL, 794, L14
Johnson, M. D., Fish, V. L., Doeleman, S. S., et al. 2015, Sci, 350, 1242
Johnson, M. D., & Gwinn, C. R. 2015, ApJ, 805, 180
Krichbaum, T. P., Graham, D. A., Bremer, M., et al. 2006, JPhCS, 54, 328
Lu, R.-S., Krichbaum, T. P., Eckart, A., et al. 2011, A&A, 525, A76
Markoff, S., Bower, G. C., & Falcke, H. 2007, MNRAS, 379, 1519
Mościbrodzka, M., & Falcke, H. 2013, A&A, 559, L3
Mościbrodzka, M., Falcke, H., Shiokawa, H., & Gammie, C. F. 2014, A&A, 570, A7
Narayan, R. 1992, RSPTA, 341, 151
Narayan, R., & Goodman, J. 1989, MNRAS, 238, 963
Narayan, R., Yi, I., & Mahadevan, R. 1995, Natur, 374, 623
Psaltis, D., Özel, F., Chan, C.-K., & Marrone, D. P. 2015, ApJ, 814, 115

Reid, M. J., Menten, K. M., Brunthaler, A., et al. 2014, ApJ, 783, 130
Rickett, B. J., Coles, W. A., & Bourgois, G. 1984, A&A, 134, 390
Shen, Z.-Q., Lo, K. Y., Liang, M.-C., Ho, P. T. P., & Zhao, J.-H. 2005, Natur, 438, 62
Spitler, L. G., Lee, K. J., Eatough, R. P., et al. 2014, ApJL, 780, L3

Thompson, A. R., Moran, J. M., & Swenson, G. W. 2007, Interferometry and Synthesis in Radio Astronomy (New York: Wiley)
Whitney, A. R., Beaudoin, C. J., Cappallo, R. J., et al. 2013, PASP, 125, 196
Yuan, F., Quataert, E., & Narayan, R. 2003, ApJ, 598, 301
Yuan, F., Shen, Z.-Q., & Huang, L. 2006, ApJL, 642, L45